Heterogeneous nucleation and growth of the β(Ti) phase in the Ti–Al system—experiments and model calculations

2009 J. Phys.: Condens. Matter 21 464111

(http://iopscience.iop.org/0953-8984/21/46/464111)

IOP Publishing Journal of Physics: Condensed Matter

J. Phys.: Condens. Matter **21** (2009) 464111 (7pp) doi:10.1088/0953-8984/21/46/464111

Heterogeneous nucleation and growth of the β(Ti) phase in the Ti–Al system—experiments and model calculations

Daniel Gosslar[1], Christian Hartig[1], Robert Günther[1], Ulrike Hecht[2] and Rüdiger Bormann[1]

[1] Institute of Materials Science and Technology, Hamburg University of Technology, Eissendorfer Straße 42, D-21073 Hamburg, Germany

[2] RWTH-Aachen, Access eV, Intzestraße 5, D-52072 Aachen, Germany

E-mail: daniel.gosslar@tu-harburg.de

Received 22 April 2009
Published 27 October 2009
Online at stacks.iop.org/JPhysCM/21/464111

Abstract

The barrier to heterogeneous nucleation of the β(Ti) phase on TiB_2 and other borides has been evaluated using the plane to plane matching model. The results are compared to the known nucleation of the α(Ti) phase on the β(Ti) phase. According to this comparison, the barrier to heterogeneous nucleation of the β(Ti) phase on TiB_2 can be judged to be small. This is in agreement with inoculation experiments. The addition of a Ti–Al–TiB_2 master composite to a β(Ti) solidifying TiAl based alloy leads to a significantly refined microstructure. Microsegregations enable us to attribute this refinement to refined equiaxed β(Ti) dendrites. However, model calculations based on the hemispherical cap model predict that the refinement via heterogeneous β(Ti) nucleation should be more potent. First calculations indicate that structural imperfections of TiB_2 particles limit the nucleation site diameter. Thereby, the nucleation barrier is increased and the refinement is less pronounced.

1. Introduction

Casting of TiAl based alloys is a promising near net shape technology. It has been successfully applied to produce low pressure turbine blades [1] and turbocharger wheels [2]. However, the formation of large columnar grains is difficult to avoid, since it is highly sensitive to the alloy composition and processing conditions.

Therefore, grain refinement of these alloys is very important. So far, this can been achieved via the addition of XD™ processed master composites containing TiB_2 particles within a porous Al matrix [3]. Hereby, TiB_2 acts as a grain refiner. Nevertheless, microstructure control is still problematic, since the grain refinement mechanism of TiB_2 is not well understood. For large contents (>1 vol%) TiB_2 remains stable in the melt and grain refinement is always observed [4]. From casting experiments on TiAl based alloys which solidified via the cubic β(Ti) phase, Saqib *et al* [5] conclude that this refinement is caused by heterogeneous nucleation on TiB_2 inoculants. However, this conclusion is based solely on a phenomenological treatment of this problem. The heterogeneous nucleation and growth of the β(Ti) phase in the Ti–Al system requires fundamental research which has not been carried out yet. The purpose of this paper is therefore to evaluate the heterogeneous nucleation barrier of β(Ti) on TiB_2 and other possible stable borides in the Ti–Al–B system. TiB_2 particles are incorporated into a Ti–Al melt via a master composite. The resulting microstructure is analysed to identify the possible heterogeneous β(Ti) nucleation. Model calculations based on the TiB_2 particle size distribution, cooling rate, alloy composition and TiB_2 content will be used to predict the β(Ti) grain size resulting from heterogeneous nucleation.

2. Modelling

The β(Ti) grain size is predicted as a function of cooling rate, alloy constitution, TiB_2 content and particle size distribution by applying the hemispherical cap model introduced by Greer

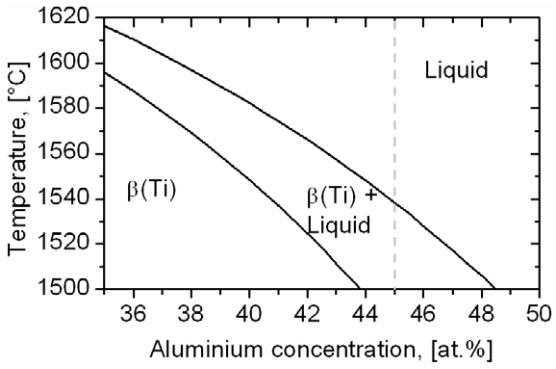

Figure 1. Section of the Ti–Al phase diagram. The dashed line indicates the nominal alloy composition.

et al [6]. The essence of this model is that a nucleus becomes supercritical as soon as its radius of curvature equals the inoculant particle radius. Thus, free grain growth is initiated for hemispherical nuclei. This model is able to predict quantitatively the grain size of inoculated CP (commercial purity) Al [6] and Mg–3Al (mass%) [7–9] alloys.

In this work, the calculation of nucleation and subsequent growth is carried out according to Günther *et al* [8]. The calculation starts with a given distribution density function of particle diameters $\rho(d, t = 0)$. $\rho(d, t = 0)$ is determined by the frequency counts of TiB_2 particles. With initiation of free grain growth, $\rho(d, t)$ evolves with time, obeying a conservation law for the number of particles coupled with an energy balance of the latent heat release of crystallization [7]. The diffusion controlled growth rate of supercritical nuclei is calculated using the concentration dependent function S introduced by Aaron and Fainstein [10]:

$$S = \frac{2(C_{\mathrm{IL}} - C_0)}{C_{\mathrm{IS}} - C_{\mathrm{IL}}} \tag{1}$$

where C_{IL} and C_{IS} are the solute concentrations at the solid–liquid interface in the melt and solid, respectively, and C_0 is the nominal alloy concentration. For alloys such as CP Al and Mg–3Al (mass%) it is reasonable to approximate this function by a linear dependence of the solute concentration on temperature. However, for Ti–45Al at.% with a high solute (Al) concentration this assumption is only approximately valid. Figure 1 shows that the β-solidus (C_{IS}) and liquidus (C_{IL}) curves exhibit a nonlinear dependence in the Ti–Al system. Therefore, a power series expansion of these curves is implemented in the hemispherical cap model enabling the grain size prediction.

Table 1 lists the input parameters used for the model calculations. The thermodynamic parameters (ΔH_V, ΔS_V and c_{PV}) are evaluated from the updated database of the Ti–Al system [11]. The solid–liquid interfacial energy is assumed to be approximately equal to that of liquid Ti at its melting temperature [12]. Since Al and Ti atoms are similar in size, the diffusivity of Al in a Ti–45Al melt is assumed to be equal to the self-diffusivity of liquid Ti (4×10^{-9} m s^{-1} [13]). In the present case (centrifugal casting) the actual diffusion constant is assumed to be larger, since transport of solute atoms is expected to be dominated by convection of the melt. Therefore it is increased by a factor of 2.

Table 1. Input parameters for model calculations of the β(Ti) grain size for a Ti–45Al at.% alloy.

Quantity, symbol	Units	Value
Enthalpy of fusion, ΔH_V	J m^{-3}	1.30×10^9
Entropy of fusion, ΔS_V	J K^{-1} m^{-3}	7.25×10^5
Heat capacity of melt, c_{PV}	J K^{-1} m^{-3}	1.63×10^6
Interfacial energy solid/liquid, $\sigma_{\mathrm{S/L}}$	J m^{-2}	0.15
Diffusivity in the melt, D_{L}	m^2 s^{-1}	8.0×10^{-9}

3. Experimental details

3.1. Processing of the master composite

A Ti–45.4Al at.% + 15 vol% TiB_2 master alloy has been prepared in three processing steps to achieve a composite with a homogeneous boride distribution. 1. High energy ball milling of TiB_2 particles and pure titanium sponge granules in a Fritsch planetary ball mill (type 5). 2. Mixing of this powder blend and aluminium powder using a tumble mixer in a closed container. 3. Compacting the mixed powders to a tablet of 50 mm in diameter and 16 mm in height using a unidirectional press at room temperature. Milling and handling of the powder has been carried out under argon atmosphere in a glove box to avoid contamination by oxidation or humidity. Figure 2(a) displays the microstructure of the master composite after compaction. This microstructure exhibits clearly a homogeneous TiB_2 particle distribution within a titanium matrix embedded within a dense aluminium powder. This homogeneity is expected to avoid clustering of particles in the melt. Figure 2(b) shows the measured TiB_2 particle frequency counts obtained by a software analysis of scanning electron micrographs in backscattered electron mode (BSE) (cf figure 2(a)). The boride particles are identified by energy dispersive x-ray spectroscopy (EDX). X-ray diffraction (XRD) measurements show that the present boride structure is TiB_2. The frequency count function is fitted by nonlinear functions to calculate the distribution density function which is an important input parameter for the model calculations.

3.2. Inoculation experiments

Inoculation experiments were carried out by melting a Ti–45.4Al at.% + 15 vol% TiB_2 master composite together with Ti–45Al alloy ingot pieces by induction heating. The integral alloy composition corresponds to Ti–45Al at.% + 1.5 vol% TiB_2, or in terms of the overall boron content, Ti–45Al–2B at.%. The melt was held at 1505 °C (30 °C superheat) for 2 min before being centrifugally cast into ceramic moulds with 16 mm diameter. The cooling rate was estimated to be in the range of 5–8 K s^{-1}. A Ti–45Al reference sample without TiB_2 additions was cast under the same conditions. Figure 3(a) shows the calculated TiB_2 equilibrium volume fraction for this alloy composition as a function of temperature. These thermodynamic calculations are based on the recent Ti–Al–B phase diagram [14]. From figure 3(a) it can be seen

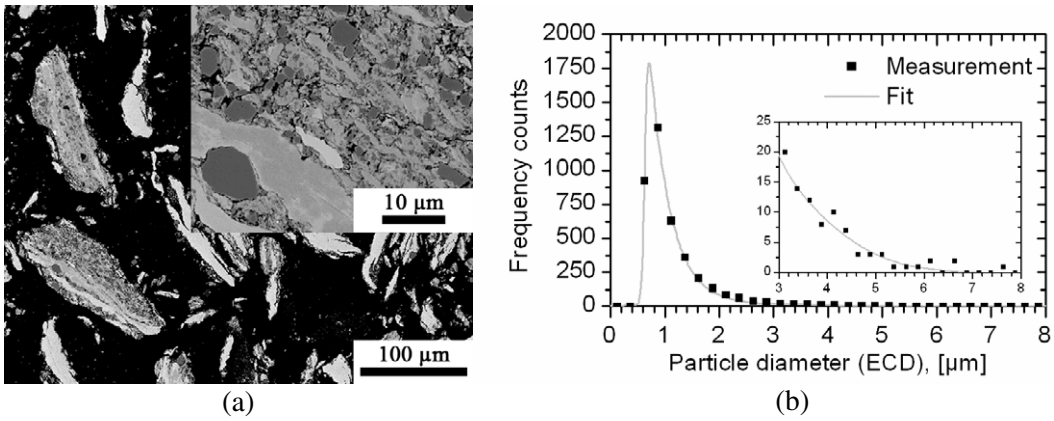

Figure 2. (a) BSE micrograph of a Ti–45.4Al (at.%) + 15 vol% TiB_2 master composite after 4 h milling. The mounting material appears black, the Ti matrix is visible by a range of grey contrasts, whereas TiB_2 is identified by a dark grey colour. (b) Measured and fitted frequency counts of TiB_2 particle diameters (equal circle diameter, ECD) based on 3860 particle counts.

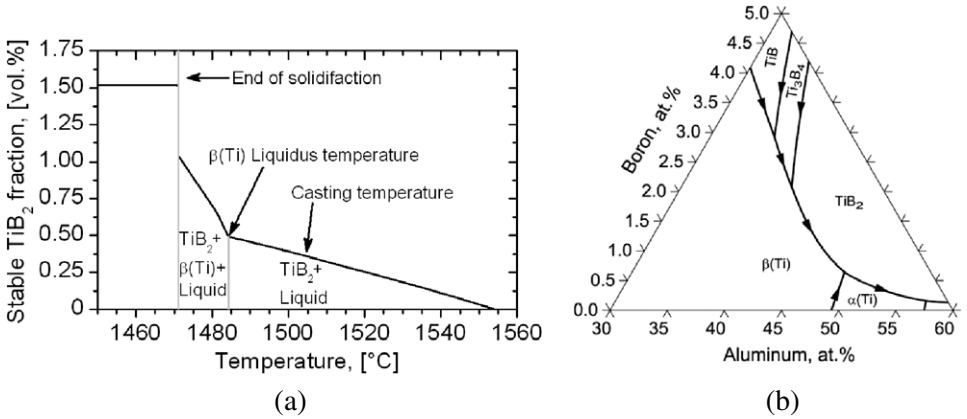

Figure 3. (a) TiB_2 volume fraction as a function of temperature for the alloy with an integral composition of Ti–45Al–2B at.%. (b) Monovariant lines in the relevant section of the projected liquidus surface of the Ti–Al–B system.

that TiB_2 does not dissolve completely in the melt if the temperature is kept lower than 1555 °C. Upon cooling from 1555 to 1480 °C, TiB_2 nuclei grow and are in equilibrium with the melt. Consequently, the stable TiB_2 fraction increases to 0.5 vol%. The casting temperature for inoculation experiments should be within this temperature range. The first β(Ti) phase starts to solidify at 1484 °C. In the temperature range from 1484 to 1470 °C the TiB_2 volume fraction increases significantly to 1 vol%. This increase occurs concurrently with the β(Ti) phase growth. Thus, growth of TiB_2 and formation of the β(Ti) phase take place at the same time. The solidification is complete below 1475 °C.

4. Results

4.1. Evaluation of the heterogeneous nucleation barrier

The plane to plane matching model is applied to determine the heterogeneous nucleation barrier of the body centred β(Ti) phase on TiB_2 which is the stable boride for the selected alloy composition (Ti–45Al–2B at.%). However, segregations during solidification can lead to the formation of borides other than the equilibrium one expected from the primary solidification fields of the Ti–Al–B system (figure 3(b)). These borides might nucleate on TiB_2 before β(Ti) solidification occurs [15, 16]. Therefore, it is also necessary to evaluate the nucleation barrier of Ti_3B_4, TiB (B27) and the metastable TiB (B_f). Additionally, segregations might cause a peritectic nucleation of the hexagonal close packed α(Ti) phase at the last stage of solidification. Consequently, the nucleation barrier of α(Ti) on the aforementioned borides is evaluated as well.

In the plane to plane matching model, parallel matching of close or nearly close packed planes is considered at the interface between nucleus and substrate. If the matching planes have a different symmetry and/or different lattice constants, the atomic arrangement of the matching nucleus plane has to be strained to obtain a fully coherent interface. This strain is called the misfit δ. With decreasing misfit it is more likely that a low energy coherent or semi-coherent interface develops, leading to a decrease of the nucleation barrier. If $\delta > 0.2$, misfit strains cannot be accommodated by misfit dislocations and strain [17] and heterogeneous nucleation is unlikely to occur. The misfit varies with crystallographic direction if the matching planes have different symmetry. The relevant misfit

Table 2. Selected titanium borides for heterogeneous nucleation of α(Ti) and β(Ti).

Phase	Crystal structure	Space group	Facets/planes
TiB_2	Hexagonal (C32)	$P6_3/mmc$	(0001), $\{10\bar{1}0\}$, $\{1\bar{2}10\}$, $\{0\bar{1}11\}$
TiB	Orthorhombic (B27)	*Pnma*	{100}
TiB	Orthorhombic (B_f)	*Cmcm*	{010}
Ti_3B_4	Orthorhombic ($D7_b$)	*Immm*	{010}

is therefore expressed correctly by the misfit strain along the principal axis of maximum strain.

The influence of aluminium concentration on the misfit strain is considered by applying Vegard's law to determine the α and β lattice constants at 47 at.% Al for the α (peritectic composition) and 41 at.% Al for the β (β phase in equilibrium with a 45 at.% Al containing melt) phase. Thermal expansion of the titanium borides and the α(Ti) and β(Ti) phases at an average temperature of 1500 °C is also included in these calculations. Possible matching planes are selected with regard to the relatively high packing densities and symmetry arguments (table 2).

First-principles calculations of Han *et al* [18] show that Ti terminated interfaces of TiB_2 offer a lower surface energy than B terminated ones if the melt is rich in Ti. Therefore, if α(Ti) or β(Ti) nucleates on TiB_2, only weak Ti–Ti interactions at the interface will occur. Consequently, the α(Ti) and β(Ti) nucleation barriers are determined primarily by the misfit.

Figure 4 shows the misfit strain δ for nucleation of α(Ti) and β(Ti) on TiB (B27), TiB (B_f), Ti_3B_4 and TiB_2. The maximum allowable misfit for catalysing heterogeneous nucleation is estimated from the known α(Ti) on β(Ti) misfit obeying the Burgers relationship [19]. It can been seen that the misfit strain for β(Ti) nucleation on TiB_2, Ti_3B_4, TiB (B27) and TiB (B_f) is well below this critical misfit of 0.17. Accordingly, the following planes/facets of titanium borides have a low nucleation barrier to β(Ti) nucleation: TiB_2-$\{10\bar{1}0\}$, TiB_2-(0001), TiB_2-$\{1\bar{2}10\}$, Ti_3B_4-{100}, TiB(B27)-{100} and TiB(B_f)-{010}. Furthermore, TiB_2 and TiB(B27) reveal also a low misfit for heterogeneous nucleation of α(Ti). Therefore, in a first assumption α(Ti) is expected to nucleate on these borides rather than on β(Ti) grains. Experimental observations by Hyman *et al* [20] reveal that dominant TiB_2 facets are of type (0001) and $\{10\bar{1}0\}$ when TiB_2 grows in a nearly equiatomic Ti–Al melt. Thus, the growth morphology of TiB_2 particles would support the refinement of β(Ti) and α(Ti).

4.2. Microstructural observations

The as cast microstructure of the Ti–45Al at.% alloy (figure 5(a)) shows coarse, fully lamellar grains (300–2000 μm). In contrast to this, the microstructure of the inoculated alloy is homogeneous with significantly refined lamellar grains, as shown in figure 5(b). Application of the line interception method for 400 grains yields a lamellar grain size of 95 μm.

The BSE micrograph of the inoculated alloy Ti–45Al at.% + 1.5 vol% TiB_2 in figure 6(a) shows that every

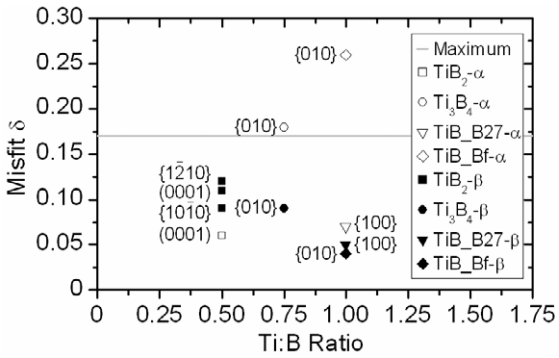

Figure 4. Nucleation barrier (expressed in terms of misfit strains δ) for α(Ti) and β(Ti) nucleation on TiB (B27), TiB (B_f) TiB_2 and Ti_3B_4. The grey line indicates the critical misfit estimated for nucleation of α(Ti) on β(Ti) following the Burgers orientation relationship.

lamellar colony is surrounded by an aluminium enriched zone (areas of dark contrast due to the lower electron density of Al compared to Ti). This enrichment stems from microsegregation during solidification. On the basis of this observation it may be conjectured that equiaxed β dendrites are similar in grain size to the lamellar colonies, with one lamellar orientation per β(Ti) dendrite. If this is true, the refinement of the microstructure is attributed directly to refined β(Ti) dendrites which is in agreement with the small crystallographic misfit between β(Ti) and TiB_2 (figure 4). However, the above argument needs to be supported by a better mapping of the solidification path which could be achieved via minor Nb additions [21]. Figure 6(b) displays the evolution of the TiB_2 particle size distribution by comparing the distribution density of particle diameters before casting (bc) within the master composite and after casting (ac). The initial distribution density function (before casting) has become broader after casting and the fraction of particles larger than 1 μm has increased. This change is caused by dissolution of small particles. Upon cooling and solidification, dissolved TiB_2 particles precipitate from the melt, nucleating on the remaining TiB_2 particles (>2 μm). Consequently, the fraction of larger TiB_2 increases. Section 4.3 discusses the influence of the aforementioned on the heterogeneous nucleation of β(Ti).

4.3. Model calculations

Calculations from figure 3(a) yield that the initial volume content of 1.5 vol% which is required for a partial stability of TiB_2 particles is reduced to an equilibrium fraction of about 0.36 vol% at the casting temperature. Figure 7(a) shows two different approaches by which this change in TiB_2 volume fraction can be incorporated into the model calculation via the distribution density functions $\rho(d)$ given in figure 6(b). Either $\rho(d)$ is multiplied by a constant factor (α) or it is shifted by a constant factor (k) to yield the equilibrium volume. The latter approach is physically more reasonable, since this corresponds to particle shrinkage instead of disappearance. Particles smaller than k dissolve completely and particles larger than k shrink by the amount of k. Obviously, this dissolution model

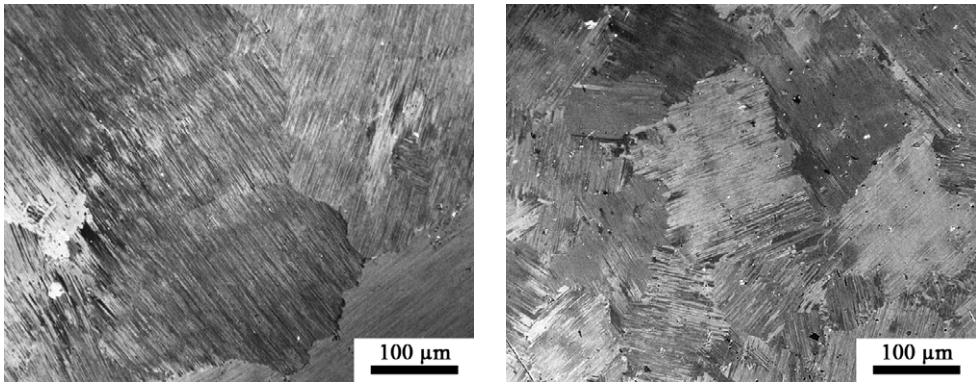

Figure 5. Optical micrographs of as cast microstructure of Ti–45Al (at.%) without (a) and with (b) TiB_2 additions of 1.5 vol%.

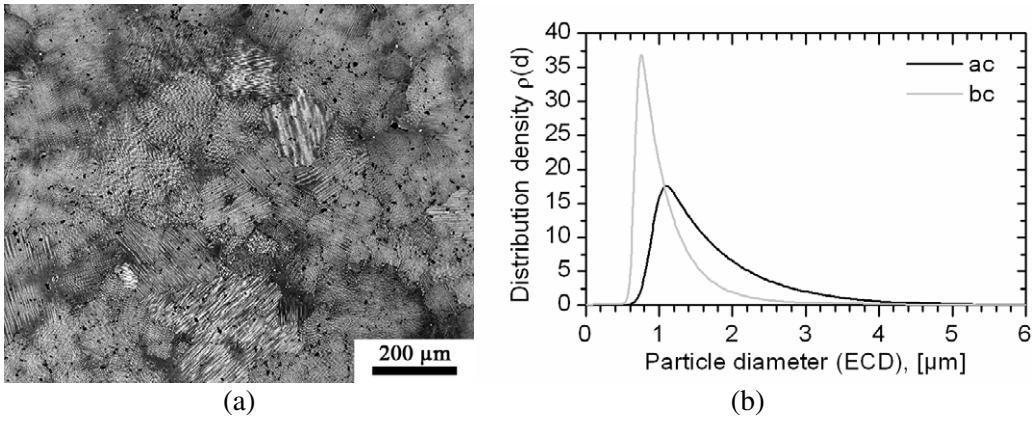

Figure 6. (a) As cast microstructure of the inoculated alloy Ti–45Al at.% + 1.5 vol% TiB_2 in BSE contrast. Black dots are identified as TiB_2 particles using EDX and XRD. (b) Distribution density functions $\rho(d)$ of the TiB_2 particle diameters (equal circle diameter, ECD) before (bc) and after casting (ac). These functions are given in arbitrary units.

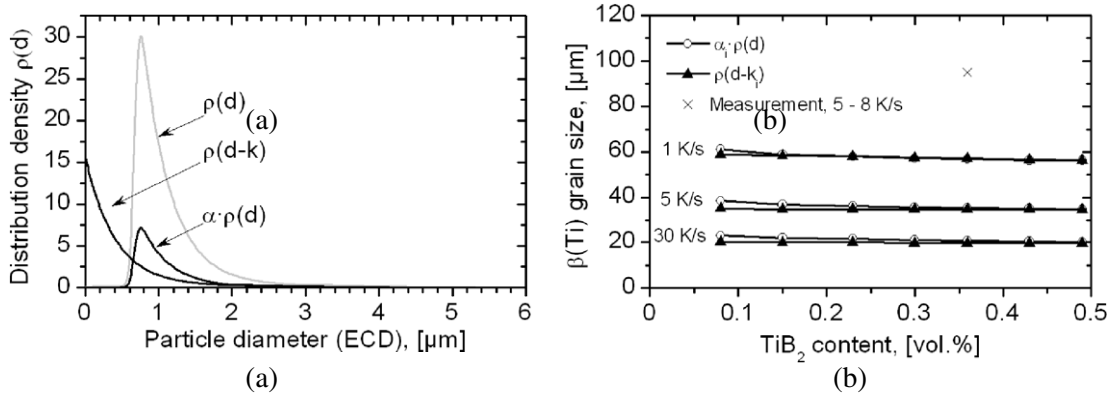

Figure 7. (a) Distribution density function $\rho(d)$ of TiB_2 particle diameters before casting (arbitrary units). The distribution corresponds to 1.5 vol% TiB_2. The transformations $\rho(r-k)$ and $\alpha\rho(d)$ yield the same equilibrium volume content. (b) Model predictions of the β(Ti) grain size as a function of TiB_2 content and cooling rate. This calculation is based on the distribution density function (figure 6(b)) of TiB_2 particle diameters before casting using the transformations shown in (a).

is very simple, since it assumes a constant dissolution velocity irrespective of the particle radius. Therefore, it can only be used to give a rough approximation. Figure 7(b) displays the predicted β(Ti) grain size for TiB_2 volume contents allowed within the temperature range of 1484 to 1555 °C stability range. The calculations are carried out for three different cooling rates (1, 5 and 30 K s^{-1}). It can be seen that the predicted grain size depends only very little on the model of dissolution. Likewise, the dependence of the β(Ti) grain size on the TiB_2 content is very small. These results change only

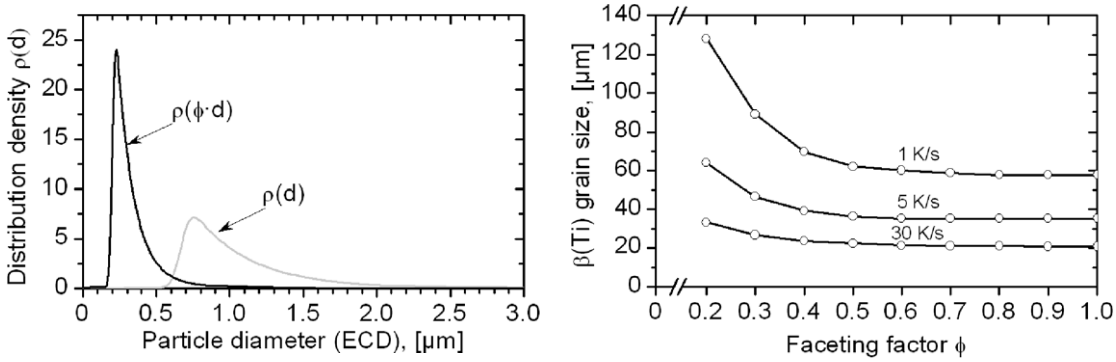

Figure 8. (a) Transformation of the distribution function $\rho(d)$ by a faceting factor ϕ towards smaller particle diameters to account for a limiting particle diameter available for heterogeneous β(Ti) nucleation. (b) Model predictions of the β(Ti) grain size as a function of the faceting factor ϕ for a constant volume fraction of TiB_2 of 0.36 vol% at three different cooling rates (1, 5 and 30 K s^{-1}). The particle dissolution is incorporated by the dissolution model of type $\alpha\rho(d)$ (cf figure 7(a)).

by a few micrometres if $\rho(d)$ for TiB_2 particle diameters after casting (figure 6(b)) is used. An explanation for the smallness of the effect of these influences on the predicted β(Ti) grain size can be given via the relatively high TiB_2 contents. This results in a saturation behaviour with a minor influence of the peculiarities of the distribution density function $\rho(d)$.

The model underestimates the measured grain size for the estimated cooling rates (5–8 K s^{-1}) by more than a factor of 3. β(Ti) grain sizes of 37 μm (5 K s^{-1}) to 30 μm (8 K s^{-1}) are predicted, while experimental results yield around 90 μm. Thus, the refinement via heterogeneous β(Ti) nucleation on TiB_2 should be much larger. Figure 7(b) has shown that the TiB_2 dissolution prior to β(Ti) nucleation has only a minor influence. Therefore, it can be assumed that this discrepancy is caused by imperfections of the nucleation sites. The source of these imperfections could be: (i) fracture surfaces originating from the preparation of the master composite by intensive ball milling; (ii) growth of unfavourable TiB_2 facets, e.g. $\{0\bar{1}11\}$, having a large nucleation barrier for β(Ti) due to misfit strains >0.3; (iii) growth of thin layers of borides other than TiB_2 on the $\{10\bar{1}0\}$ facets of TiB_2 [15, 16], thereby preventing β(Ti) nucleation. These imperfections would limit the effective nucleation site diameter for heterogeneous nucleation. This can be introduced into the model calculation by a 'faceting factor' ϕ which is the ratio of the effective particle diameter d_{eff} to the real particle diameter ($\phi = d_{\mathrm{eff}}/d$). The effective distribution density function $\rho'(d_{\mathrm{eff}})$ then results from a transformation $d_{\mathrm{eff}} = \mathrm{d}\phi$ under the condition of the conservation of the particle number. Figure 8(a) displays such a transformation. Figure 8(b) displays first model calculations for ϕ in the range of 0.2 (severely limited nucleation sites) to 1.0 (perfect nucleation sites). The model predictions yield an increasing β(Ti) grain size with decreasing ϕ. This is caused by the transformed distribution density function leading to the initiation of grain growth at a greater undercooling. It can be seen from figure 8(b) that the effective diameter should be limited to being less than 20% ($\phi = 0.2$) of the particle diameter, in order to achieve an agreement with the experimentally measured grain size in the range of 5–8 K s^{-1}. Clearly the TiB_2 imperfections have to be confirmed by experiments. It is therefore important to analyse the TiB_2 morphology by electron microscopy (TEM/HRTEM) in great detail. This will help us to understand the interplay between the morphology of TiB_2 inoculants and the grain refinement achieved.

5. Conclusions

Experimental verification of β(Ti) nucleation on TiB_2 particles was achieved by casting a Ti–45Al at.% alloy after melting together with a Ti–45.4Al at.% + 1.5 vol% TiB_2 master composite. The final grain size of the resulting alloy Ti–45Al at.% + 15 vol% TiB_2 was about an order of magnitude lower than that of a reference casting with boride-free Ti–45Al at.%. Microstructural observations suggest that this refinement is caused by heterogeneous β(Ti) nucleation on TiB_2 inoculants. Modelling results indicate that the grain refinement via heterogeneous β(Ti) nucleation should be much more pronounced, i.e. the refinement is a factor of 3 less than that observed experimentally. It is concluded that this can be explained by severely limited nucleation site diameters of TiB_2 particles due to structural imperfections.

Acknowledgment

The authors gratefully acknowledge the financial support by the German Research Foundation (DFG) within the SPP No. 1296 priority programme.

References

[1] Austin C M and Kelly T J 1999 *Gamma Titanium Aluminides* ed Y-W Kim *et al* (Warrendale, PA: TMS) pp 21–32
[2] Noda T 2008 *Gamma Titanium Aluminides and Other Metallic Aluminides* ed Y-W Kim *et al* (Warrendale, PA: TMS) p 7
[3] Brupbacher J M, Christodoulou L and Nagle D C 1987 *US Patent Specification* 4,710,348
[4] Larson D E 1990 *Intermetallic Matrix Composites* vol 194, ed D L Anton *et al* (Pittsburgh, PA: MRS) pp 285–92

[5] Saqib M, Weiss I, Mehrotra G M, Clevenger E, Jackson A G and Lipsitt H A 1991 *Metall. Trans.* A **22** 1721–8
[6] Greer A L, Bunn A M, Tronche A, Evans P V and Bristow D J 2000 *Acta Mater.* **48** 2823–35
[7] Günther R, Hartig C and Bormann R 2006 *Acta Mater.* **54** 5591–7
[8] Günther R, Hartig C and Bormann R 2008 *Magnesium Technology 2008* ed M O Pekguleryuz *et al* (Warrendale, PA: TMS) pp 95–9
[9] Günther R, Hartig C, Hort H and Bormann R 2009 *Magnesium Technology* 2009 ed M O Pekguleryuz *et al* (Warrendale, PA: TMS) pp 309–13
[10] Aaron H B, Fainstein D and Kotler G R J 1970 *J. Appl. Phys.* **41** 4404–10
[11] Witusiewicz V T, Bondar A A, Hecht U, Rex S and Velikanova T Y 2008 *J. Alloys Compounds* **465** 64–77
[12] Allen B C 1972 *Liquid Metals: Chemistry and Physics* ed S Z Beer (New York: Dekker) p 186
[13] Bellot J P, Foster B, Hans S, Hess E, Ablitzer D and Mitchell A 1997 *Metall. Mater. Trans.* B **28B** 1001–10
[14] Witusiewicz V T, Bondar A A, Hecht U, Zollinger J, Artyukh L V, Ya T and Velikanova T Y 2009 *J. Alloys Compounds* **474** 86–104
[15] Graef M D, Loefvander J P A, McCullough C and Levi C G 1992 *Acta Metall. Mater.* **40** 3395–406
[16] Kitkamthorn U, Zhang L C and Aindow M 2006 *Intermetallics* **20** 1–11
[17] Frank F C and van der Merwe J H 1949 *Proc. R. Soc.* A **198** 216–25
[18] Han Y, Dai Y, Shu D, Wang J and Sun B 2006 *Appl. Phys. Lett.* **89** 144107
[19] Burgers W G 1934 *Physica* **1** 561–86
[20] Hyman M E, McCullough C, Levi C G and Mehrabian R 1991 *Metall. Trans.* A **22A** 1647–62
[21] Chen G L, Xu X J, Teng Z K, Wang Y L and Lin J P 2007 *Intermetallics* **15** 625–31